Dang et al. EURASIP Journal on Image and Video Processing (2018) 2018:105
https://doi.org/10.1186/s13640-018-0351-1

EURASIP Journal on Image and Video Processing

RESEARCH Open Access

Detection imaging of impulse borehole well-logging radar

Longfei Dang*, Hongchun Yang and Baohua Teng

Abstract

Borehole ground-penetrating radar (hereinafter referred to as GPR) technology is a geophysical detection method in the well, in which, the high-frequency electromagnetic waves are transmitted to stratum and the spread properties of electromagnetic waves in the stratum are used to obtain stratum information, thereby interpreting the subsurface structures. Based on the basic principle of target detection, a set of borehole GPR was developed in this paper. Many detection experiments were conducted on this radar system, and fairly good imaging results were obtained, indicating the superior performance of impulse system-based UWB radar in geological research and mining exploration.

Keywords: Imaging results, Impulse borehole well-logging radar, Target detection

1 Introduction

Impulse radar is highly valuable to engineering design and development of high-tech military, civil radar, and other systems (including four-resistance radar, wall- or ground-penetrating radar, jungle radar, precision guidance radar, time-domain proximity fuse, borehole well-logging radar, and geological disaster monitoring radar). Compared to continuous wave radar, impulse radar has many advantages, such as a simple structure, low interception, high resolution, electromagnetic interference resistance, and a strong anti-stealth ability. Borehole geological exploration radar is an impulse system radar which is based on the generation, transmission, radiation, receiving, data collection, data processing, and imaging of impulse signals. It identifies the position or shape of the target object by accurately measuring the time difference and the waveform parameter difference of the electromagnetic signals reflected by the target object, and it is a typical impulse system-based ultra-wide band radar (hereinafter referred to as UWB). The major information carriers of its target detection are the time-domain impulse waveform parameters and the time information between time-domain time impulses, so it is also called the time-domain radar. The impulse radar is of great value to the engineering design and development of high-tech military, civil radar or system (including four-resistance radar, wall- or ground-penetrating radar, jungle radar, precision guidance radar, time-domain proximity fuse, borehole well-logging radar, and geological disaster monitoring radar) [1–12].

The major advantages of impulse borehole well-logging radar include:

(1) Strong penetrating ability, long transmission distance
Currently, mature boreholing methods are adopted for exploring the geological structure, such as the current method, resistivity method, ultrasonic method, X-ray method, and ray method, and the radial detecting distance of all these existing instruments is less than 70 cm. After the time-domain radar concept of the impulse system is put forward, the radial detecting distance of the geological exploring radar can be increased dramatically under the appropriate electromagnetic parameter (r), environment, as the center frequency of nanoseconds even the nanosecond electromagnetic pulse (Gaussian waveform) is still at 100 MHz magnitude and has a strong penetration ability in rocks or common stratum medium environment (especially in the medium environment with low conductivity). For example, in the limestone formation $< 10^{-5}$, the radial detecting distance of the impulse radar can reach 102–103 m magnitude.
(2) High resolution

* Correspondence: ttyygg1666@163.com
School of Physics, University of Electronic Science and Technology of China, Chengdu 610054, China

According to the theory of continuous electromagnetic wave radar, the radar resolution depends on its operating bandwidth which with the same wavelength corresponding to the radar center frequency normally. Therefore, the center frequency has to be increased in order to improve the radar resolution, thus greatly reduce the detecting distance of radar, and vice versa. On the basis of the Rayleigh criterion of time-domain radar theory, the impulse radar resolution depends on the pulse width of time-domain electromagnetic pulse. For the electromagnetic pulse of ns magnitude, its resolution is about 15 cm in the air, about 2 cm in water environment, and about 8 cm in coal medium which has higher resolution compared with the common continuous meter-wave radar. The high resolution of impulse radar can also be explained by continuous wave radar theory, since the operating bandwidth of impulse radar is usually greater than 100%, even more than 200%, wider than 25% operating bandwidth of the ultra-wide band continuous wave radar; it is with high resolution.

(3) Low average power, simple structure, and low costs
The average power of impulse radar system is normally at moment magnitude (mW), with low average power and low consumption, and is easy to realize system miniaturization and more suitable for deep geological environment with high temperature. Meanwhile, the impulse radar mainly uses the electromagnetic pulse time information, and the corresponding circuit is with simple structure and low cost.

As compared with the earth ground-penetrating radar, the borehole GPR can obtain more abundant information of deep geological mining resource, so it is the most effective means to obtain and detect complex geological mining structures. The researches of radar for detecting shallow strata and underground targets have a history of 100 years [13]. According to the radar application environment, geological exploration radar can be divided into airborne ground-penetrating radar, ground or shallow ground tunnel radar, and drill-hole deep-underground type drill-hole radar. From the aspect of technical methods to realize geological exploration, the geological exploration radar can be divided into blasting detection method [14], acoustic wave detection method [15], current detection method (resistance method), ray detection method (X-ray, Y-ray) [16], and electromagnetic wave detection method [17], etc. At present, except the electromagnetic radar method, the detection range of other test methods is very limited, and the detection range reported in the literature does not exceed 176 cm. Electromagnetic wave geological exploration methods are divided into continuous wave detection radar and impulse detection radar. The underground exploration radar based on continuous wave system has the defects of low resolution and short transmission distance. Therefore, the geological exploration radar based on impulse system has become a hot research topic in this field. The borehole logging radar based on impulse system has a wide detection range, high resolution, and relatively low cost and has a broad market demand prospect. Not only that, it also has broad application prospects in many hot application fields such as coal mine water penetration accident detection, through-wall and ground-penetrating radar, geological and seismic disaster prediction, and even mineral resource exploration. The key technologies of the impulse system geological exploration radar mainly include high stability, low trigger jitter electric signal source, Omani-directional, directional ultra-wide band antenna, transmission characteristics of impulse signals in complex media, data processing and imaging of impulse electromagnetic signals, electromagnetic compatibility within the impulse radar system, and electromagnetic matching between the impulse radar and the application environment, etc. Among them, the transmission characteristics of time-domain electromagnetic pulses in complex media [18, 19], the development of directional time-domain antennas, the electromagnetic compatibility of the system, and the matching between the system and the environment are the difficult technologies in the development of impulse geological exploration radar. It is among these key technologies that this paper has done a lot of researches and experiments on signal data processing and imaging and has obtained some good experimental results.

The following chapters are divided into several parts. Section 2 introduces the target positioning principle. Section 2.2 demonstrates the radar system indexes. Section 3.1 introduces the radar as a whole. Section 3.2 introduces experimental test for antenna frequency-domain parameter. Section 3.3 introduces experimental data of antenna time-domain parameters. Section 3.4 introduces experimental and imaging processing. Section 4 introduces the conclusion.

2 Method

On the one hand, the development trend of wireless communication technology from broadband to narrowband, and narrowband to broadband again, shows that using impulse system radar to detect the target location or distribution represents the latest development trend and the direction of this field, which is with advancement and innovation in theoretical and technical schemes. There are few relevant research reports or product introduction in domestic, and the active ultra-wide band radar currently is also a hot research

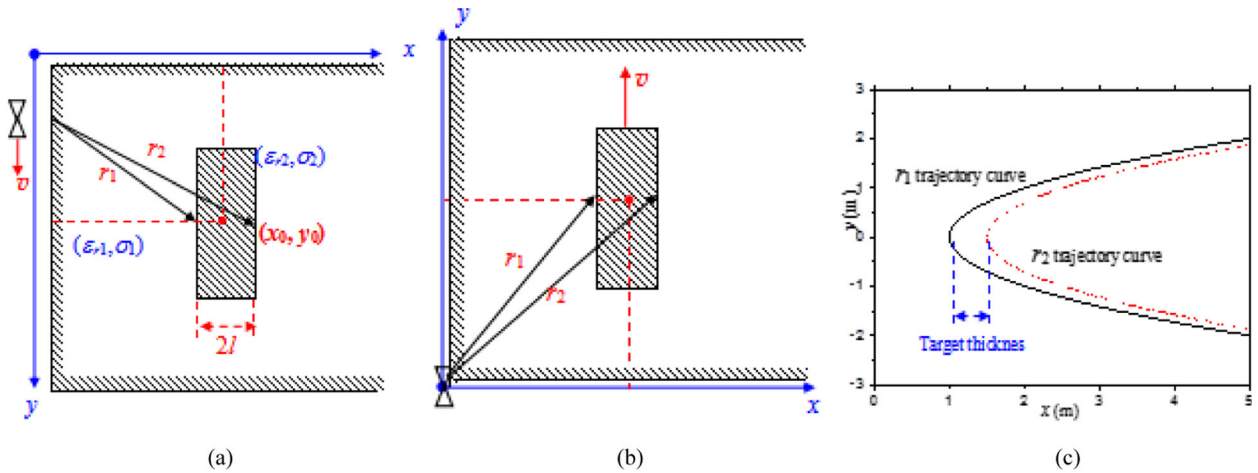

Fig. 1 The principle calculation model of target detection. **a** Moving antenna model. **b** Moving target model. **c** Target trajectory curve

field worldwide; on the other hand, as the existing geological exploration instrument has serious limitations on detecting distance or resolution, adopting the time-domain radar research scheme with penetration ability and high may be one of the most effective solutions to such instrument limitation. Due to lack of theoretical analysis methods and engineering experience in many aspects, for example, transmission theory of impulse signal in complex media is still at developing stage, the electromagnetic compatibility issue, the matching problem of radar system under different environments, and recognition and judgment problems of impulse radar imaging, it is determined that the project research must be combined with applied basic theory research and extensive engineering experiments. In other words, the practical technical difficulties in engineering practice will be resolved via applied basic theoretical analysis, and the new analysis scheme of applied basic theory will be put forward through experimental test results.

2.1 Basic principles of target detection

The principle calculation model of target detection was shown in Fig. 1. When the radar system was detecting the target object, the moving target detection host was used to draw the target object trajectory curve (as shown in Fig. 1a, c) with the host as the reference system. Then, the spatial coordinates of the target were obtained from the trajectory curve by the focus algorithm. As the calculation model of target object trajectory curve, it was obvious that the calculation model of Fig. 1a can be replaced with Fig. 1b.

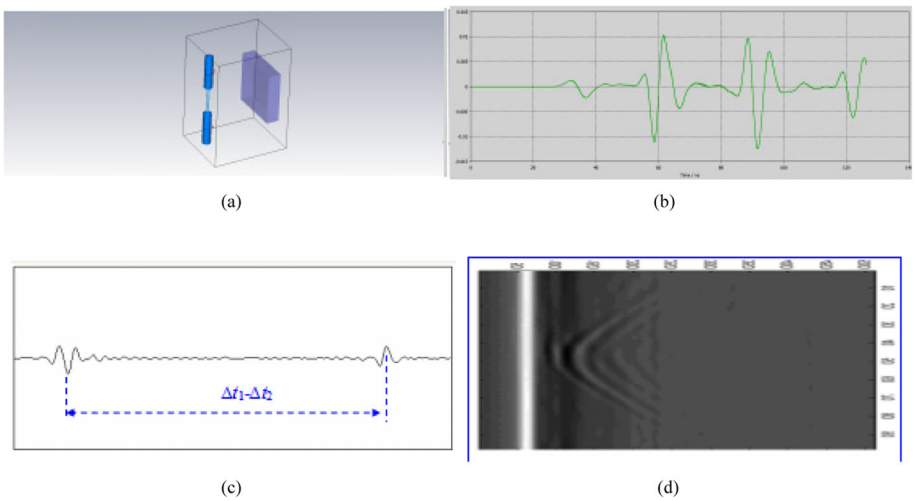

Fig. 2 Target echo signal and imaging diagram. **a** CST simulation calculation model for target echo signal. **b** CST simulation calculation results for target echo signal. **c** Experimental test results for interface echo signal. **d** Target position and shape diagram after DC and noise wave removal

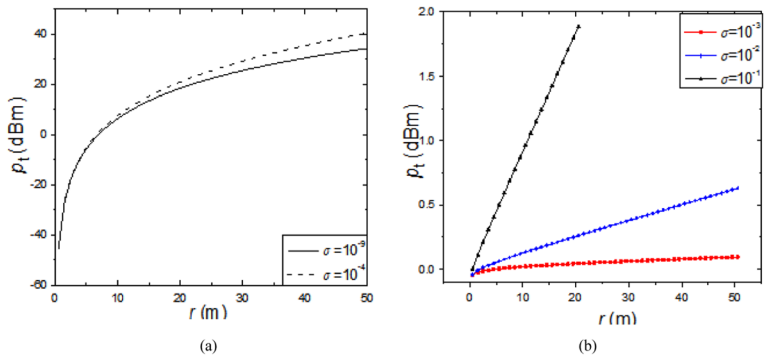

Fig. 3 p_t-r changes under differences: **a** p_t-r changes under minor and **b** p_t-r changes under major

Set the antenna along the y-axis (or target object along the y-axis) in a uniform motion at velocity v, the dielectric constant of the environment medium was ε_{r_1}, the conductivity was σ_1, the dielectric constant of target object was ε_{r_1}, the conductivity was σ_1, the vector at reflection center position of two reflectors in target object medium was r_1 and r_2, respectively. According to Fig. 1b, the trajectory equation for the center point of reflector can be written as

$$\begin{cases} y_1 = \sqrt{\dfrac{c^2\Delta t^2}{4\varepsilon_{r_1}} - (x_0 - l)^2} \\ \dfrac{c\Delta t}{2} = \sqrt{\varepsilon_{r_1}\left[(x_0 + l)^2 + y^2\right]} + \left(\sqrt{\varepsilon_{r_2}} - \sqrt{\varepsilon_{r_2}}\right)\sqrt{\left[\dfrac{2ly}{x_0 + l}\right]^2 + 4l^2} \end{cases} \tag{1}$$

where Δt represents the time difference between the host trigger signal and the target object echo signal.

The terminal trajectory curve diagram for position vector r_1 and r_2 was shown in Fig. 1c. When there was a target object with certain thickness in the environment medium, two curves would be displayed on the interface after the data processing, and the position and thickness parameters of the target object can be obtained by the focus imaging on these two curves. The interface imaging diagram for echo signal time-domain waveform and after DC removal was shown in Fig. 2 when there was target object.

2.2 The radar system indexes

2.2.1 Detection distance of radar system

According to the radar equation in frequency domain, the received power and radiant power of transient electromagnetic pulse shall be satisfied after transmitting via air and medium as follows.

$$\frac{p_r}{p_t} = \frac{G_t G_r \gamma_{01}\gamma_{10}\lambda_0^2 S}{(4\pi)^3 r^4}\ \exp(-4\alpha \cdot r) \tag{2}$$

The relationship between detection distance and P_t is shown in Fig. 3. When the electromagnetic wave enters vertically, the loss tangent of the formation is as follows:

$$\tan\delta = \sigma/\omega\varepsilon << 1 \tag{2}$$

$$\gamma_{01} = \gamma_{10} \approx \frac{4\sqrt{\varepsilon_{r_1}}}{\left(1 + \sqrt{\varepsilon_{r_1}}\right)^2} \tag{3}$$

Thereinto, P_r is the received power; P_t is the transmitted power; G_t and G_r is the receiving and transmitting antenna gain, respectively; λ_0 is the wavelength of the electromagnetic wave in the air; S is the radar cross section of the target; r is the target depth; γ_{01} and γ_{10} are the coupling coefficients of the receiving and transmitting antenna, and the ground, respectively, and are the formation attenuation factors.

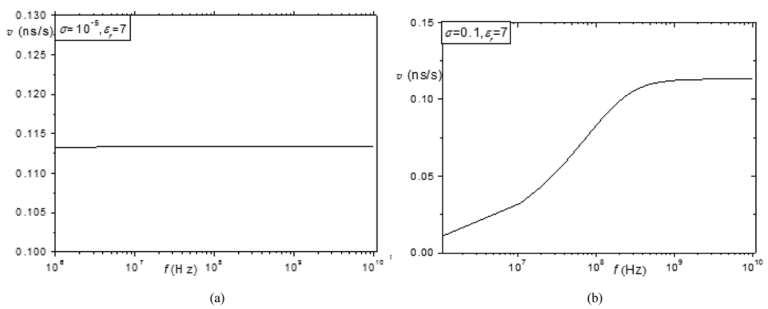

Fig. 4 Changes of the transmission speed of electromagnetic waves vary with frequency. **a** v-f changes under minor and **b** v-f changes under major

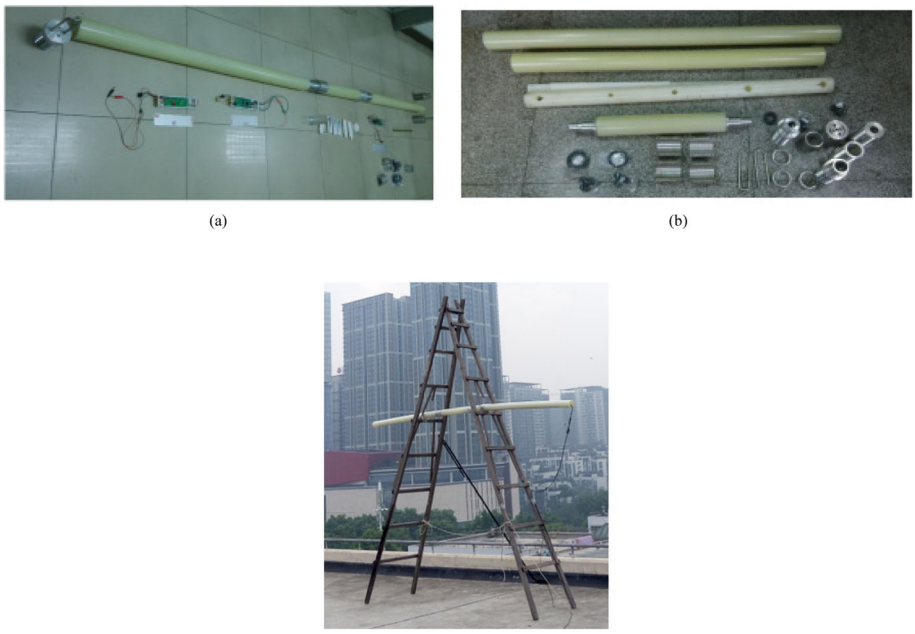

Fig. 5 The material object of the mechanical structure design of the drilling and logging radar. **a** The material object illustration. **b** The main mechanical structural components of the radar system. **c** The complete system photos

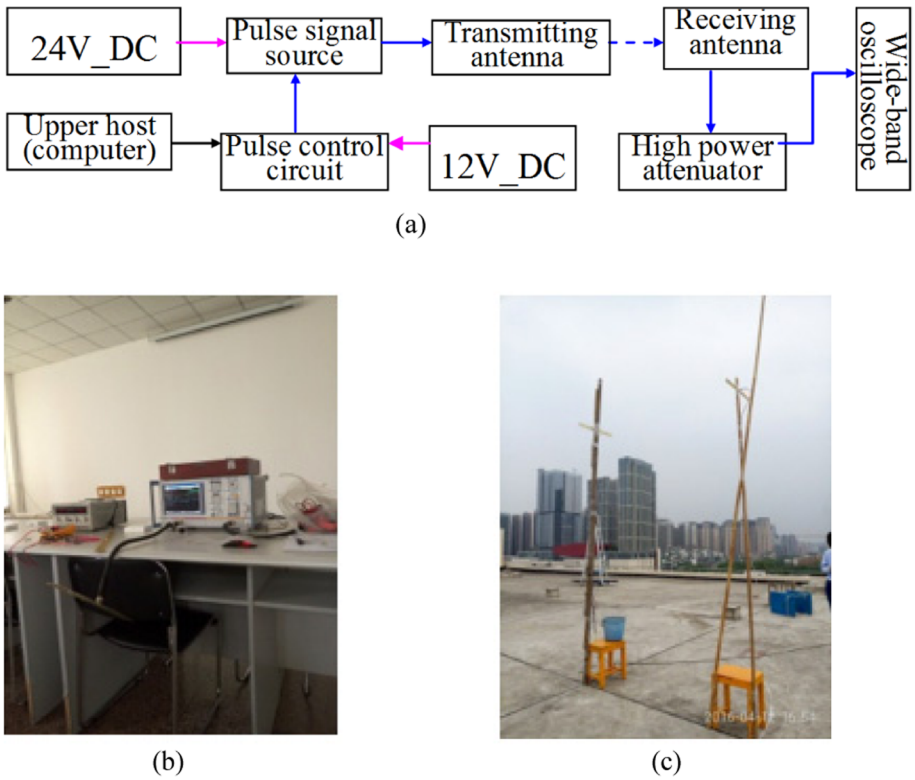

Fig. 6 Test circuit diagram and onsite photo of receiving antenna parameters. **a** Schematic diagram of time-domain parameters test circuit for receiving antenna. **b** Test photo of frequency-domain parameters. **c** Test photo of time-domain parameters

The minimum detectable power of the receiver $P_{r\min}$ is

$$P_{r\,\min} = k_0 T \Delta f \cdot F(S_0/N_0)_{\min} \tag{4}$$

Thereinto, k_0 is the Boltzmann constant, T is the working ambient temperature of the receiver, Δf is the equivalent noise passband, F is the noise figure of the receiver, and $(S_0/N_0)_{\min}$ is the minimum detectable signal-to-noise ratio of identified target.

2.2.2 Calculation of radar resolution

According to sharpness criterion, the calculation formula of radar radial resolution is

$$\delta_r = \frac{\tau \cdot c}{2\sqrt{\varepsilon_r}} \tag{5}$$

Thereinto, τ is the pulse width of the radar electromagnetic pulse, c is the light transmission speed in the air, and r is the dielectric constant of the limestone. According to the theoretical calculation and preliminary test results of the transient electromagnetic pulse radiated from the ultra-wide band antenna radiation: after the antenna radiation, the waveform of *1.5*-ns first-order Gaussian electromagnetic pulse is approximate to the second-order Gaussian electromagnetic pulse with *5*-ns pulse width. Then put the theoretical calculation and preliminary test results into Formula (5), and the radar radial resolution in the coal seam can be derived $\delta_r = 50$ cm; for water-course ($\varepsilon_r = 81$), the resolution is $\delta_r = 17$ cm.

2.2.3 Radar unambiguous distance

The calculation formula of minimum radar unambiguous distance is the same as of Formula (5); therefore, its value is also 50 cm. The calculation formula of maximum radar unambiguous distance is

$$\delta_R = \frac{cT}{2} \tag{6}$$

Thereinto, T is the repetition frequency of the electromagnetic pulse beam emitted by radar system. If the chosen is $R = 10$ km, then $1/T < 15$ kHz is required.

2.2.4 Transmission speed of electromagnetic wave in formation

The calculation formula for the transmission speed of electromagnetic wave in the formation is

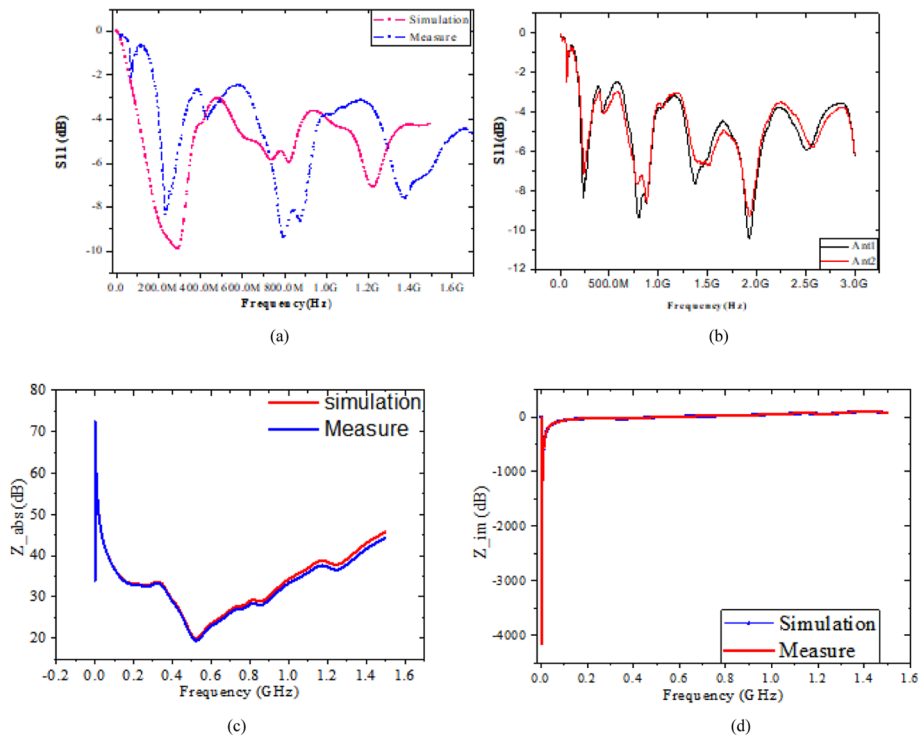

Fig. 7 The antenna *S* parameters, impedance, and the simulating calculation. **a** Comparison of antenna *S* parameter simulation and test results. **b** Test comparison of *S* parameter consistency of receiving and transmitting antenna. **c** Comparison of real-part simulation and test results of antenna impedance. **d** Comparison of imaginary part simulation and test results of antenna impedance

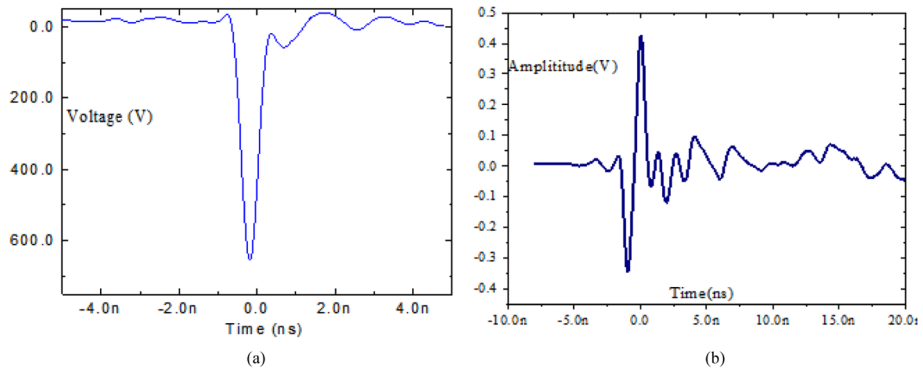

Fig. 8 Feed pulse waveform and the typical signal waveform received by receiving antenna. **a** Feed pulse waveform of pulse signal source. **b** Typical pulse signal waveform received by receiving antenna

$$v = \frac{\omega}{\beta} \tag{7}$$

$$\beta = \omega\sqrt{\mu\varepsilon}\left\{\frac{1}{2}\left[\sqrt{1+\left(\frac{\sigma}{\omega\varepsilon}\right)^2}+1\right]\right\}^{1/2} \tag{8}$$

According to Formula (7), the v relationship shown in Fig. 4 can be calculated.

Through the preliminary demonstration or calculation of the aforesaid technical parameters of radar system, we can find that the realization of various technical parameters proposed by the project research institute is feasible.

3 Results and discussion

3.1 The whole radar system

In this section, the entire radar system was used to do a lot of tests or experiments, making preparations for the imaging processing step by step. The following picture was the complete system photos.

Figure 5 gives the material object of the mechanical structure design of the drilling and logging radar. Figure 5b gives the main mechanical structural components of the radar system, including transmitter cylindrical tube (1 m), receiver cylindrical tube (1 m), hollow tube for regulating the gap between the transmitter and receiver (each bushing section is 1 m long), fixing support of radar transmitter and receiver components, and sealing nut. Figure 5a gives the material object illustration after the radar system is assembled. The minimal length of the whole system is 3 m, and the maximal length is 4 m depending on the length of the regulating hollow tube (including 1-section or 2-section regulating hollow tube). The system diameter is 900 mm.

Test the S parameters of single receiving and transmitting antenna, and the impedance parameter (real part, imaginary part) by the vector network analyzer. Test the time-domain waveform and time-domain directional diagram of single receiving and transmitting antenna radiation.

Antenna parameter, time-domain directional diagram, and onsite testing photos are shown in Fig. 6.

3.2 Experimental test for antenna frequency-domain parameter

Connect the testing circuit and check according to Fig. 6a. Fix the receiving and transmitting antenna onto the receiving and transmitting antenna support, respectively, (with the same distance to the ground) and record the ground clearance h. Take the pivot of the transmitting antenna support as the center, draw the arc with radius r on the ground (r shall be determined to ensure that the direct wave signal can be identified with the ambient reflection signal), and record r. Take the point at the equal central angle on the arc and place the pivot of the receiving antenna support on the testing point of equal central angle successively. Test and record the waveform data received by the receiving antenna.

Figure 7 shows the antenna S parameters, impedance, and the simulating calculation; thus, it can be seen that the simulating calculation of the antenna frequency-

Table 1 Main parameters for the electromagnetic pulses of time-domain antenna radiation

Quantity	Numerical value
Testing distance (m)	2
Amplitude (mV)	872.5
Peak width of main peak (ns)	0.871
Pulse width (ns)	1.96
Trailing range (mV)	150
Trailing time (ns)	2

Note: The antenna height above the ground is $h = 2.5$ m; To test the axis radiation, each data is the average of 128 tests

Table 2 Test data for the time-domain directional diagram

Angle (°)	Single source E	Single source H
15	931.2	872.0
30	732.8	834.6
45	587.7	832.8
60	443.2	837.0
75	319.0	849.0
90	292.3	819.0
105	388.9	848.0
120	477.5	801.8
135	507.0	782.8
150	561.6	768.1
165	763.9	770.7
180	869.2	763.5

Note: The test data under different angle is the amplitude of radiation signal, unit mV

domain parameter is in accordance with the test results within a margin of error.

3.3 Experimental data of antenna time-domain parameters

(1) Experimental test of electromagnetic pulse waveform parameters radiated from single antenna

Figure 8 shows the feed pulse waveform of transmitting antenna, receiving and transmitting antenna (same antenna) radiation and received typical signal waveform; Table 1 shows the test results of the receiving signal waveform parameter of the receiving antenna.

(2) Experimental test of time-domain directional diagram of single antenna

Test data for the time-domain directional diagram of single antenna refers to Table 2, and data processing results refer to Fig. 9.

The frequency-domain and time-domain parameters have completed the expected indicators, e.g., center frequency of receiving and transmitting antenna (according to the time-domain antenna − 6 dB as the standard), time-domain gain, amplitude ratio of trailing signal, and E-plane time-domain directional diagram. The test result of receiving and transmitting antenna bandwidth is 0.2–0.3 GHz and 0.7–1 GHz (according to the time-domain antenna − 6 dB as the standard). The test result of trailing signal lasting time is 2 ns, meeting the expected indicator 3 ns. The antenna impedance test value is 40–140 Ω, meeting the expected project indicator 40–150 Ω.

Compared with the literature report results, great progress has been made in key parameters of the receiving and transmitting antenna subsystem such as time-domain gain, operating bandwidth, and trailing inhibition. The electromagnetic compatibility problems of receiving and transmitting antenna subsystem and front-end signal pulse source, back-end receiver can be effectively solved by adding the attenuator, but if so, the effective output amplitude of the pulse source decreases, and thus, the detection range reduces. In order to solve this problem, the original output amplitude of the pulse source can be increased.

3.4 Experimental and imaging processing

We simply extract the target information by using the time alignment, amplitude normalization, and time-varying amplification and use the corresponding data processing program compilation method. All of the results are directly from our system. The impulse radar system adopts the time-domain waveform

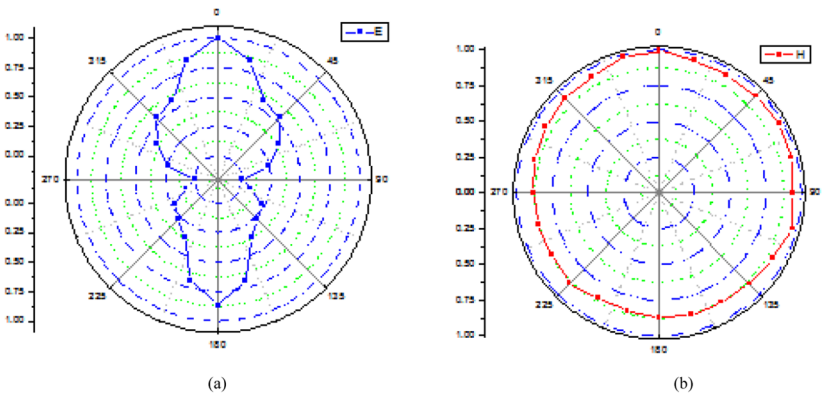

Fig. 9 Experimental test result of time-domain directional diagram of single receiving antenna. **a** Test result of pulse signal source in E-plane directional diagram. **b** Test result of pulse signal source in H-plane directional diagram

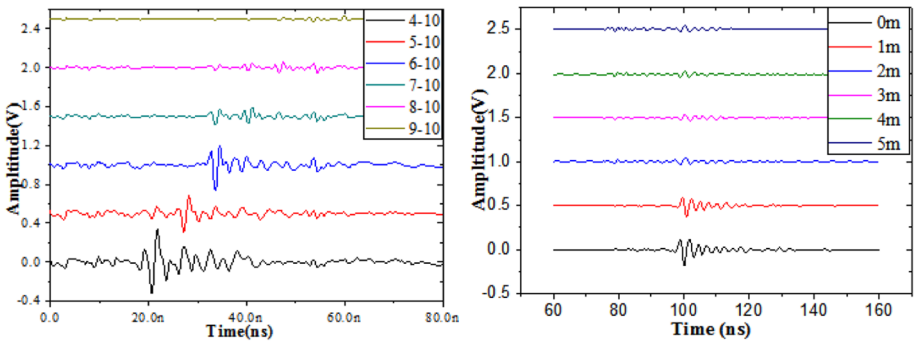

(a) (b)

Fig. 10 Signals received by moving target. **a** Perpendicular to system moving target. **b** Parallel to system moving target

correlation reception method to detect the target. Combined with the working characteristics of the experimental prototype system developed in this paper, the radar system is initially stationary, and the ambient clutter remains unchanged for a short time. Secondly, the received signal is a time-domain signal, which is convenient to suppress and even eliminate the signal of random noise. Accordingly, we propose the following object information extraction method. Firstly, the characteristic point of the direct wave signal of the transmitting antenna and receiving antenna is used as the reference point of the starting point of the system timing. Secondly, environmental noise signal background is collected in advance. Thirdly, the environmental noise signal is removed from the echo signal containing the target information, and the effective information of the target is obtained. We call this method a time-domain radar data processing method. All experiments were conducted in the same radar system without using any known detection system.

3.4.1 Early experiments

Figure 10 showed that the target echo received by the oscilloscope was being used by the system. As can be seen from the figure, when the target was perpendicular to the system, as shown in Fig. 10a, due to the close distance and large distance change in moving, the target echo signal was more obvious, and there was more significant movement on the time axis. When the target was parallel to the system, as shown in Fig. 10b, because the target was far away from the system and the receiving antenna was far from the transmitting antenna, the echo signal was obvious only when target was on the system midperpendicular; however, when the target was deviated from the system midperpendicular, the echo signal was decreased rapidly.

Figure 11 showed that the oscilloscope was used by the system to receive the signal from receiving antenna, and then, the signal was processed in MATLAB to obtain the imaging results. Figure 11a showed the imaging results when the target was moving perpendicular to the system, and Fig. 11b showed the imaging results when

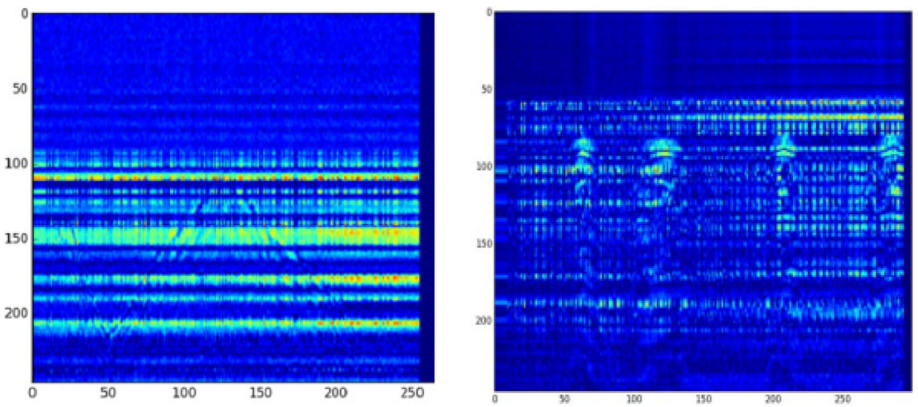

(a) (b)

Fig. 11 Imaging results received by moving target. **a** The imaging results when the target was moving perpendicular to the system. **b** The imaging results when the target was moving parallel to the system

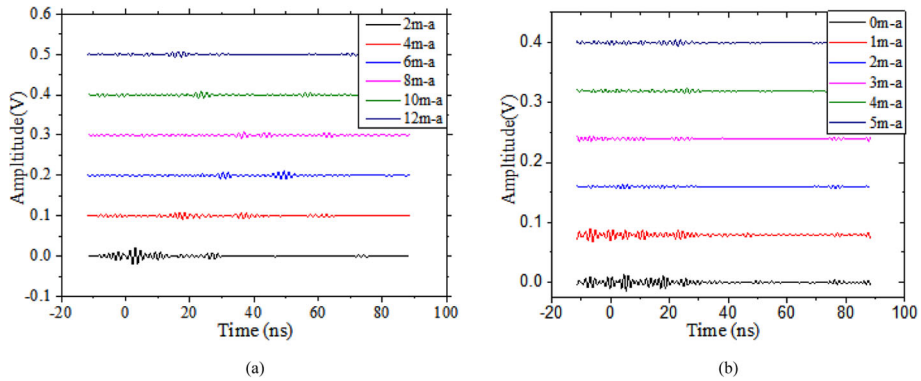

Fig. 12 Signals received by moving antenna. **a** Perpendicular to moving antenna. **b** Parallel to moving antenna

the target was moving parallel to the system. The trajectory formed by the target movement can be clearly seen from the figure. There was a clear horizontal stripe in Fig. 11a, which was the interference caused by the multiple reflections due to the poor matching between the pulse source and the transmitting antenna. The attenuator was added for matching in the in Fig. 11b experiment, and such interference was basically eliminated.

Figure 12 showed the signals collected by the oscilloscope of fixed target moving system from the receiving antenna. Figure 12a showed the signal received when perpendicular to the target moving system, and Fig. 12b showed the signal received when parallel to the target moving system. It can be seen from the figure that the signal received in moving target was much weaker than that of the fixed system, and the reason was that background environment was continuously changing when the system was moving, so it was difficult to detect useful signals from the background.

Figure 13 showed the imaging results when fixed target was perpendicular and parallel to moving system. By introducing the background sliding averaging window, the target image formed by the moving system can be seen clearly from the figure, and the effect was good. Background sliding averaging window dynamically averaged a number of original echo signals and used them as background signals. Since the background signal change was irrelevant when the system was moving, the averaging was able to effectively reduce the background noise and improve the imaging quality.

3.4.2 Imaging experiment

Limestone or granite was selected as the geology of experimental, while thickness of soil covering the rock should not exceed 5 m. There should be at least 30–40 m high cliff on experimental site, and the cliff surface should be relatively vertical; at the same time, there should be at least 50 m^2 relatively flat open space on the cliff. As shown in Fig. 14a, two wells were drilled on the experimental site. Well no. 1 was 67-m deep, and no. 2 was 48-m deep. The distance between the centers of two wells was 2.7 m. The centerline of the two wells was parallel to the cliff and was 13 m away from the cliff. As shown in Fig. 14b, the cliff was about 80 m high, and its surface was smooth, satisfying the experimental requirements.

Figure 15 showed the close-up photos of wellhead of test well and the sample photos of borehole rock core. Wellhead diameter was 11 cm, and the geological structure distribution in the well: 1–4 m was the soil, 4–32 m was the granite, 32–40 m was the yellow

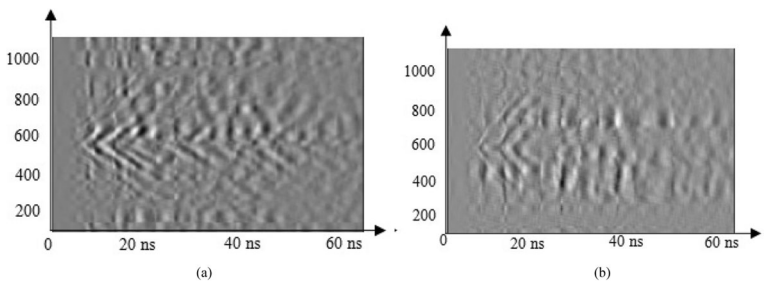

Fig. 13 Imaging results for fixed target moving system. **a** Imaging results when perpendicular to moving system. **b** Imaging results when parallel to moving system

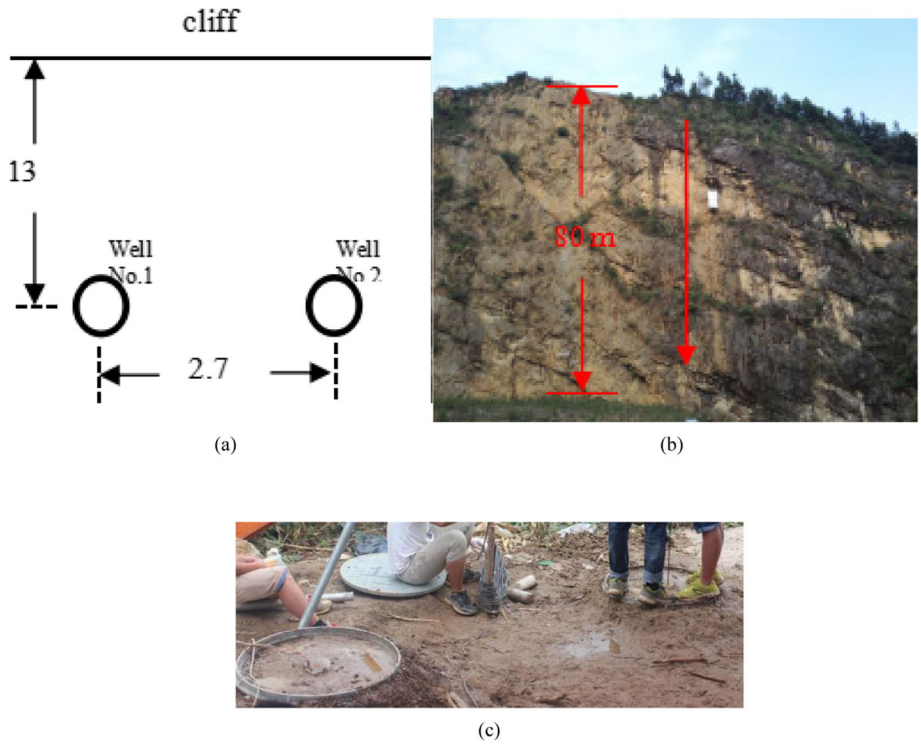

Fig. 14 Borehole diagram. **a** Borehole position diagram. **b** Cliff height and borehole relative position. **c** Wellhead field photos

sandstone, and 40–60 m was the granite. Due to the rainy season during drilling, there was a lot of rainwater in the well, with 17-m water depth in well no. 1 and 31-m water depth in well no. 2.

Radar system test was also divided into two parts. The first part was the cross-hole transmission wave test, namely, the radar system was lowered into the well no. 1, and the receiving antennas was used to receive signals in the well no. 2, observing the waveform radiated by transmitting antenna. The second part was the single-hole reflection imaging experiment, namely, the radar system was lowered from 7 m depth in well no. 1 to continuously measure to 35 m depth, and the measurement time window was 20–160 ns. The test site photos and cross-hole test waveforms were shown in Fig. 16a, b, respectively.

As can be seen from the cross-hole test waveforms in Fig. 16b, the received signal was a similar first-order Gaussian pulse, with amplitude about 135 mV and main pulse duration about 10 ns.

The second part of imaging experiment was a real-time single-hole reflection imaging experiment. Since the time window of the system was short, only 60 ns, and the vertical lowering depth was also spliced, namely, the 7–35 m length was divided into two measurements, so a complete image was composed of six parts. In order to ensure the repeatability of the experiment and to eliminate the false signals caused by

Fig. 15 Close-up photos of wellhead and sample photos of rock core. **a** Wellhead photos. **b** Rock core photos

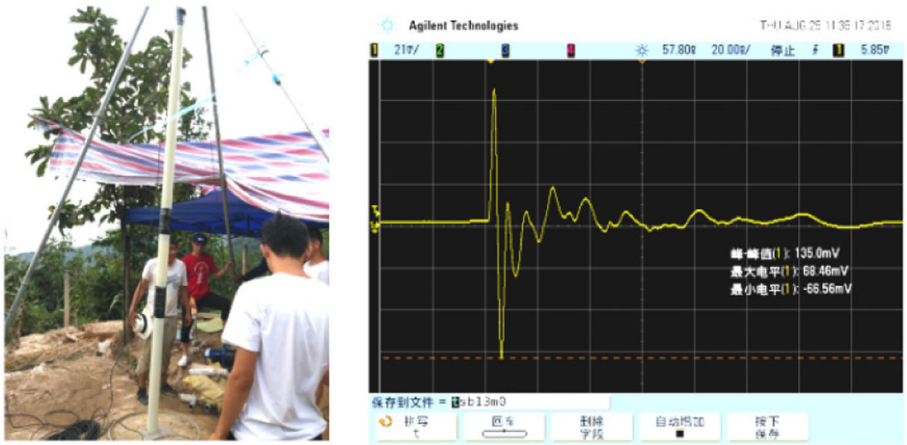

Fig. 16 Test site photos and cross-hole test waveforms. **a** Experimental test site. **b** Cross-hole test waveforms

external interference and system's own noise waves, two tests were carried out when the system ran from top to bottom from 7 to 35 m. Moreover, the feature points of each test result were compared to ensure the validity of the experiment.

The imaging results of the first measurement from top to bottom from 7 to 35 m were shown in Fig. 17. It can be seen that due to the high frequency and narrow impulse width, this borehole well-logging radar had a higher resolution than the existing radar systems on the market, so it can explore more details.

In order to illustrate the validity of the geological structure detection results around well no. 1, the test results at different times and different modes were put together for comparison, and some obvious feature points were selected for the comparison in detection position and shape, thereby verifying the experimental results.

Figure 17 showed the first test results from top to bottom from 7 to 35 m. There were 7 obvious feature points in the figure in total. Feature point 1 was located on abscissa 20–40 ns and ordinate 7–10 m, feature point 2 was located on abscissa 50–72 ns and ordinate 8–16 m, feature point 3 was located on abscissa 75–85 ns and ordinate 7–14 m, feature point 4 was located on abscissa 95–110 ns and ordinate 14–21 m, feature point 5 was located on abscissa 22–60 ns and ordinate 28–34 m, feature point 6 was located on abscissa 79–91 ns and ordinate 23–31 m, and feature point 7 was located on abscissa 110–140 ns and ordinate 20–28 m.

Figure 18 showed the result of the second test from top to bottom. As can be seen from the figure, the seven feature points corresponding to Fig. 17 were all found in Fig. 18, and both target shape and position were well matched.

Figures 19 and 20 are the double imaging results of the radar system when moving downwards from 35 to 7 m. It can be seen that the two figures have 7 characteristics corresponding to Figs. 17 and 18, and the shape, time axis position, and depth of these characteristics are basically compatible which means these targets exist indeed, not the false signals caused by external interference or system clutter.

The farthest feature point on the time axis in the imaging results was point 7, locating at 110–140 ns.

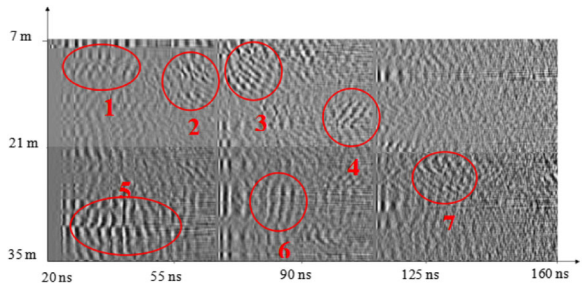

Fig. 17 First measurement from top to bottom

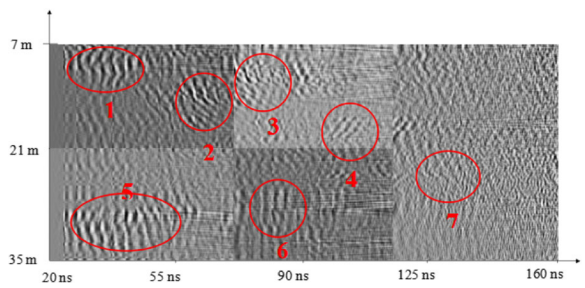

Fig. 18 Second measurement from top to bottom

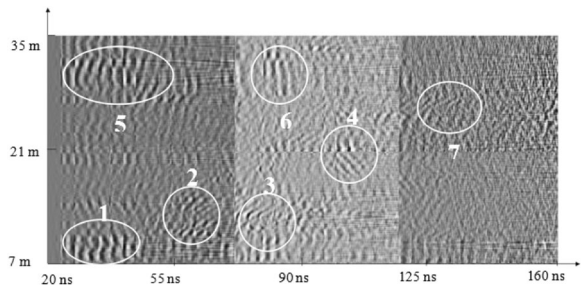

Fig. 19 First measurement from bottom to top

As the typical relative dielectric constant of granite was 6, the farthest effective detection distance of the radar can be calculated to be about 8.5 m. The experimental time was the local rainy season, and there was relatively large water content in the stratum, so the maximum detection distance was affected. Should the measurement be conducted in the dry geological conditions, a better result was expected to be obtained. It can improve the amplitude of the output source and improves the effective transmission capability of the antenna. The electromagnetic compatibility method suitable for the ultra-wide band impulse system shall be studied to improve the disturbance resistance of the whole system. The signal processing and target imaging algorithm under complicated geological environment shall be studied to effectively recognize target features. The mechanical structures shall be improved to improve the system hardness and water resistance.

4 Conclusions

This radar system verified the capability of the impulse system-based UWB borehole well-logging radar to explore the geological conditions around the well and indicated the superior performance of the impulse system-based UWB radar in geological research and mining exploration, laying a good foundation for the following work. The whole radar system is relatively complete, the detection results are better, and the imaging is clear and visible and can be further developed and improved. Of course, due to the lack of accumulation in signal processing and target imaging study in complex geological environment, there was still a lot of improvement space in imaging effect. We validate the investigation capabilities of the ultra-wide band drilling and logging radar based on impulse mechanism for the geological conditions around the well via experiments. It embodies excellent performance of the ultra-wide band radar based on the impulse mechanism in geological research and mineral investigation and lays solid foundation for next work.

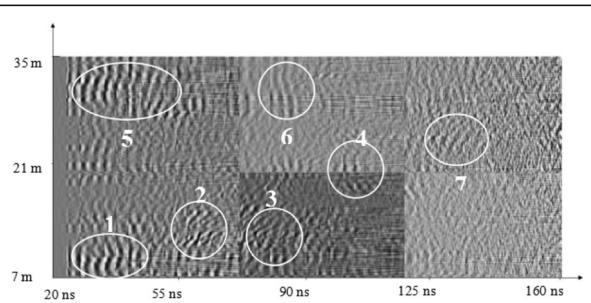

Fig. 20 Second measurement from bottom to top

Abbreviations

GPR: Ground-penetrating radar; UWB: Ultra-wide band

Acknowledgements

The authors thank the editor and anonymous reviewers for their helpful comments and valuable suggestions.

About the authors

Long Fei Dang* received the B.Sc and M.Sc. degrees in applied mathematics from Chengdu University of Information Technology, China, in 2010 and 2013, respectively. In 2014, he joined the School of Physics, University of Electronic Science and Technology of China, for the Ph.D. degree in condensed matter physics. His research interests include time-domain antenna, impulse signal, radar system, and imaging of time-domain radar. He is a correspondence author.

Hong Chun Yang received the B.Sc. degree in physics from Sichuan Normal University, in 1989; the M.Sc. degree in field theory and particle physics from Sichuan University, in 1997; and the Ph.D. degree in electromagnetic field and microwave technology from University of Electronic Science and Technology of China, in 2008. Since 1997, he has been a teacher with the School of Physics, University of Electronic Science and Technology of China. He is involved in research on UWB signal source, UWB antenna, UWB radar system and application, complex electromagnetic environment, and complex network research.

Bao Hua Teng received the B.Sc. degree in physics from Hohai University, in 1982; the M.Sc. degree in physics from Xian Jiaotong University, in 1986; and the Ph.D. degree from Sichuan University, in 2002. Since 2005, he has been a professor with the School of Physics, University of Electronic Science and Technology of China. He is involved in research on condensed matter physics, theoretical physics, and quantum computation.

Availability of data and materials

We can provide a part of the data.

Author's contributions

All authors take part in the discussion of the work described in this paper. The author LFD wrote the first version of the paper and did a part of the experiments of the paper. HCY and BHT revised the paper in different versions of the paper, respectively. All authors read and approved the final manuscript.

Ethics approval and consent to participate

Approved.

Consent for publication

Approved.

Competing interests

The authors declare that they have no competing interests. And all authors have seen the manuscript and approved for submission. We confirm that the content of the manuscript has not been published or submitted for publication elsewhere.

Publisher's Note

Received: 1 August 2018 Accepted: 30 September 2018
Published online: 16 October 2018

References

1. H. Nickel, F. Sender, R. Theirbach, H. Weichart, Improved geophysical radar-probing equipment for boreholes. Geophysics. **47**(4), 413–417 (1982)
2. H. Nickle, F. Sender, R. Thierbachm, et al., Exploring the interior of salt domes from borehole. Geophys. Prospect. **31**(1), 131–148 (1983)
3. W. Dail, Underground oil-shale retort monitoring using geotomography. Geophysics. **49**(10), 1701–1707 (1984)
4. K.A. Dines, R.J. Lytle, Computerized geophysical tomography. Proc. IEEE. **67**(7), 1065–1073 (1979)
5. R.J. Lytle, E.F. Laine, D.L. Lager, D.T. Davis, Cross-borehole electromagnetic probing to locate high-contrast anomalies. Geophysics. **44**(10), 1667–1676 (1979)
6. H.J. Cui, H.C. Yang, C.L. Ruan, Propagation characteristics of arrayed transient electromagnetic pulses. Chin. Sci. Bull. **56**(18), 1957–1964(2011)
7. A.M. Nicolson, C.L. Bennett Jr., D. La-mensdorf, L. Susman, Applications of time-domain metrology to the automation of broad-band microwave measurements. IEEE Trans. Microwave Theory Tech. **20**(1), 3–9 (1972)
8. L.D. DiDomenico, A comparison of time versus frequency domain antenna patterns. IEEE Trans. Antennas Propag. **50**(11), 1560–1566 (2002)
9. V.H. Nguyen, J.Y. Pyun, Location detection and tracking of moving targets by a 2D IR-UWB radar system. Sensors. **15**(3), 6740–6762 (2015)
10. K. Takahashi, J. Igel, H. Preetz, M. Sato, Sensitivity analysis of soil heterogeneity for ground-penetrating radar measurements by means of a simple modeling. Radio Sci. **50**(2), 79–86 (2015)
11. S.S. Tiang, M.F. Ain, M.Z. Abdullah, in *Rf & Microwave Conference*. Compact and wideband wide-slot antenna for microwave imaging system (2011), pp. 63–66
12. D Eisenmann, FJ Margetan, L Koester, D Clayton: Inspection of a large concrete block containing embedded defects using ground penetrating radar. American Institute of Physics Conference Series, 2016, **1706**(1): 1341–1348
13. H.-H. Li, Overview of ground penetrating radar system. J. Test. Technol. **17**(l), 25–28 (2003)
14. Hui Cao: Overview of borehole geophysical technology. Progress in exploration geophysics. **27**(4): 235–240(2004)
15. M. Blenkinsop, P. Baker, C. Clavier, W. Kenyon, in *SPWLA 27th Annual Logging Symposium, Paper XX*. Deep electromagnetic propagation tool interpretation (1994)
16. M. Xue, Z.-H. Chu, H. Jiang, Review on development of sonic logging tools. Pet. Instrum. **14**(5), 6–10 (2000)
17. D.J. Daniels, *Ground Penetrating Radar 22nd Edition* (The Institution of Electrical Engineers, London, 2004)
18. D. Poljak, C.Y. Tham, *Integral Equation Techniques in Transient Electromagnetics* (WIT Press, Southampton, 2003)
19. S.M. Rao, *Time Domain Electromagnetics* (Academic Press, 1999)